# scientific reports

**OPEN**

# Research on mix design and mechanical performances of MK-GGBFS based geopolymer pastes using central composite design method

Ziqi Yao[1], Ling Luo[1,2✉], Yongjun Qin[1,2], Jiangbo Cheng[1] & Changwei Qu[1]

In order to alleviate environmental problems and reduce $CO_2$ emissions, geopolymers had drew attention as a kind of alkali-activated materials. Geopolymers are easier access to raw materials, green and environment friendly than traditional cement industry. Its special reaction mechanism and gel structure show excellent characteristics such as quick hardening, high strength, acid and alkali resistance. In this paper, geopolymer pastes were made with metakaolin (MK) and ground granulated blast furnace slag (GGBFS) as precursors. The effects of liquid–solid ratio (L/S) and modulus of sodium silicate (Ms) on the performances of MK-GGBFS based geopolymer paste (MSGP) were characterized by workability, strength and microstructural tests. The regression equations were obtained by central composite design method to optimize the mix design of MSGP. The goodness of fit of all the equations were more than 98%. Based on the results of experiments, the optimum mix design was found to have L/S of 0.75 and Ms of 1.55. The workability of MSGP was significantly improved while maintaining the strength under the optimum mix design. The initial setting time of MSGP decreased by 71.8%, while both of the fluidity and 28-d compressive strength increased by 15.3%, compared with ordinary Portland cement pastes. Therefore, geopolymers are promising alternative cementitious material, which can consume a large amount of MK and GGBFS and promote green and clean production.

**Keywords** Metakaolin, Slag, Central composite design, Workability, Compressive strength

Ground granulated blast furnace slag (GGBFS) is a solid waste produced from blast furnaces during pig iron smelting. About 0.3–1.0 t of blast furnace slag is produced for every 1 t of iron produced. In China, the production of industrial solid waste was as high as 3.787 billion t in 2020, of which 0.69 billion t of metallurgical waste slag accounting for 18.19%[1]. Meanwhile, the generation of industrial solid waste is accompanied with the emission of greenhouse gases. It is estimated that the year-on-year growth of $CO_2$ emissions rose from 0.9% in the 1990s to 3% in the 2000s, while annual emissions of $CO_2$ are nearly 29.6 billion t and on an increasing trend[2,3]. The traditional cement industry accounts for about 8–9% of total anthropogenic $CO_2$ emissions[4]. To mitigate the situation, GGBFS can be considered as a raw material to produce geopolymers. Geopolymer is a kind of alkali-activated materials, which are typically made from GGBFS, metakaolin (MK), and fly ash (FA)[5–7]. These materials have excellent properties such as high compressive strength, good durability, high temperature resistance, and well acid resistance[8–11]. Compared with the production of ordinary Portland cement (OPC), the $CO_2$ emissions of alkali-activated materials can be reduced by up to 80%, ensuring material performance and achieving the aim of green and energy-saving at the same time[12].

Several attempts in different aspects have been made to broaden the application of geopolymers in the construction industry[13–17]. Based on previous research, GGBFS-based alkali-activated materials tends to have poor workability, high drying shrinkage and quick setting, while MK-based alkali-activated materials are characterized by slow setting and mitigation of the drying shrinkage[18–23]. A good synergy of GGBFS and MK in alkali-activated materials could obtain both good workability, mechanical strength and durability[23–25]. The study of Alanazi et al. pointed out that, the partial replacement of FA with MK significantly enhanced the early strength (the strength

[1]College of Civil Engineering and Architecture, Xinjiang University, Urumqi 830017, China. [2]Xinjiang Civil Engineering Technology Research Center, Urumqi 830017, China. ✉email: luoling128@126.com

at 3 days increased from 14 to 30 MPa)[26]. Zhang et al. proved that under normal temperature curing conditions, the mechanical performance of MK-based geopolymers were similar to those of OPC, and often exhibits higher flexural strength[27]. Habert et al. addressed that geopolymer concrete made from FA/GGBFS require less sodium silicate solution to activate[28]. Therefore, they have a lower environmental impact than geopolymer concrete made from pure MK.

Besides, the mix design of different precursors based geopolymer is complex, including many influencing factors, as modulus of sodium silicate (Ms), liquid–solid ratio (L/S), curing conditions, and others[29–33]. Danish et al. studied the effects of Ms and curing conditions on the properties of prepacked geopolymer mixes. The findings suggested that the specimens cured for 8 h with a given Ms performed higher compressive and flexural strength[29]. Zhang et al. found that the strongest unconfined compressive strength (UCS) of solid alkali-activated geopolymers was obtained when L/S and Ms were 0.64 and 1.16[34]. According to the research of Wang et al., the performance of FA-based geopolymer paste was effectively improved while maintaining the strength by increasing the alkali-activator, decreasing Ms, and adjusting the water-binder ratio (w/b)[35].

Response surface methodology is a collection of statistical and mathematical techniques, which achieves its goal by improving the settings of the factors, bringing the response closer and closer to the predetermined maximum or minimum value[36–38]. Response surface methodology can be used in the process of designing, developing, and building new products, as well as in improving existing products designs[39–43]. Meanwhile, the number of trials can be minimized by response surface methodology and identify the interactions between factors at-a-time[44]. Central composite design (CCD) is the most popular response surface methodology in use, in which the axial distance and the number of center runs can be flexibly selected[37,45]. Response surface methodology uses the factorial methods and Analysis of Variance (ANOVA) to model the response values. On top of this, CCD adds extra factors, both within (at the focal point) and outside of the factor region (at the star point), to highlight the results and enhance the predictive capacity of the models[46].

Many scholars used CCD to optimize the experiment process and distinguish the interactions between factors. Watson et al. identified the interactions between As and natural organic matter during the ferric chloride coagulation via CCD[44]. In order to maximum the properties of the electrospun nanofiber, Rooholghodos et al. used CCD to optimized the crosslinking duration and CQDs-$Fe_3O_4$-RE concentration[47]. Du et al. found the optimum mix proportion of high-volume FA mortar using CCD[48]. However, the studies of improving the performances of geopolymer pastes using CCD were limited.

In the present study, the MK-GGBFS binary composite system was used as the precursor to produce geopolymer paste, and L/S and Ms were selected as the experimental variables. The models of fluidity, initial setting time and UCS (3-d, 7-d, 28-d, 60-d) were established by CCD method. Then, the microstructure was characterized by SEM and XRD. Ultimately, the optimum mix design of MSGP was employed to ensure the workability and mechanical performance.

## Materials and experimentation
### Materials
The Blaine fineness of MK and GGBFS were 620 and 430 $m^2$/kg, respectively. The basicity coefficient $K_b = (CaO + MgO)/(SiO_2 + Al_2O_3)$ of GGBFS was 1.23. The OPC was Tianshan P·O 42.5R cement. The chemical compositions of these materials are listed in Table 1. The alkali-activator was prepared by mixing NaOH particles (96%) and sodium silicate solution in a certain proportion. The chemical composition of sodium silicate solution was $SiO_2$ (26.6%) and $Na_2O$ (8.7%), the original modulus was 3.16. In the trial test, the activator concentration of 36%, 37%, 38%, 39% and 40% were used, and it was easier to mix at 37%. Therefore the activator concentration was set at 37% in this study.

The microstructure of MK and GGBFS samples were characterized by Sigma-300 SEM produced by ZEISS, which was illustrated in Fig. 1. Mastersizer-2000 Laser diffraction tester produced by MALVERN examined the particle size distribution of MK and GGBFS, which were shown in Fig. 2. The D50 (average particle size) of GGBFS and FA are about 4.52 μm and 18.6 μm. Figure 3 presents the XRD patterns of MK and GGBFS. It is obvious that MK includes many crystalline phases such as quartz ($SiO_2$), kaolinite ($Al_4[Si_4O_{10}](OH)_8$), calcium silicate ($C_2S$ and $C_3S$), dolomite ($CaMg(CO_3)_2$) and muscovite ($K\{Al_2[AlSi_3O_{10}](OH)_2\}$). The humps centring at the 2θ range of 20–30° of MK and 25–35° of GGBFS reflect an amorphous phase[49,50].

### Mix design of MSGP based on CCD method
In this study, CCD method was used to investigate the effect of L/S and Ms on the performance of MSGP. According to the relevant studies and a trail test, the primary variation ranges of L/S and Ms were determined[31,34,51–54]. L/S ratios were set at 0.7, 0.8, 0.9 and 1.0, and Ms values were set at 1.2, 1.5 and 1.8. The total amount of binders were 450 g. MK and GGBFS were equal as 225 g. The control group OPC pastes had a w/b of 0.5, which using

| Materials | CaO | SiO₂ | Al₂O₃ | Fe₂O₃ | SO₃ | MgO | K₂O | Na₂O | LOI |
|---|---|---|---|---|---|---|---|---|---|
| MK | 0.65 | 51.59 | 40.05 | 2.30 | 0.41 | 2.17 | 1.57 | 0.83 | 1.88 |
| GGBFS | 43.15 | 29.20 | 12.59 | 1.44 | 2.00 | 8.09 | 0.45 | 0.52 | 0.73 |
| Cement | 56.78 | 25.52 | 7.51 | 2.89 | 2.43 | 1.33 | 0.67 | 0.49 | 1.45 |

**Table 1.** Main chemical composition of raw materials (wt%).

(a) MK

(b) GGBFS
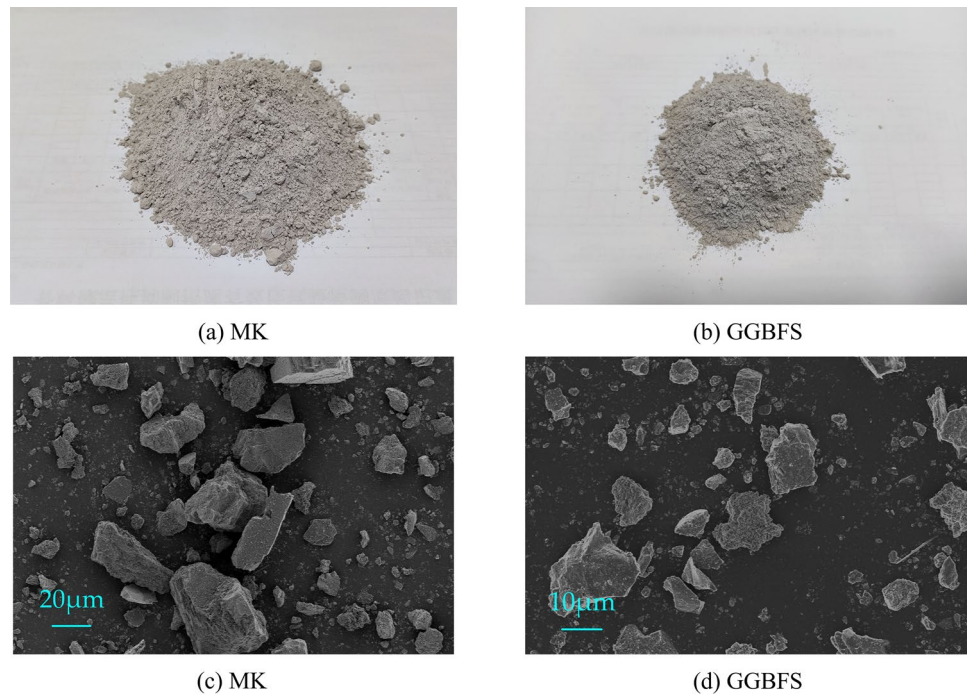
(c) MK

(d) GGBFS

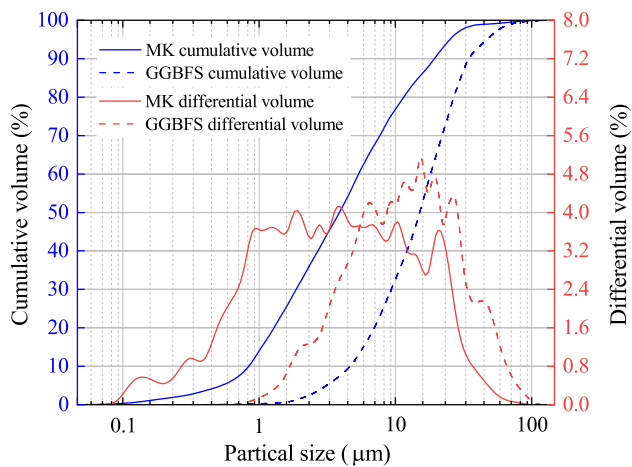**Figure 1.** Physical photo and SEM of MK and GGBFS.



**Figure 2.** Particle size curves of MK and GGBFS.

cement as binders and no admixtures. The response values are fluidity, initial setting time, and UCS (3-d, 7-d, 28-d, 60-d). Table 2 summarizes the factors, codes and levels of MSGP mix design under the CCD method.

## Experimental methods

### Setting time
MSGP was prepared according to the mix design of the CCD method. The initial and final setting times of pastes were measured referred to Chinese Standard GB/T 1346–2011[55]. The samples used to test the setting time of OPC pastes should be standard consistency ones.

### Fluidity
The fluidity tests of freshly mixed MSGP pastes were conducted according to Chinese Standard GB/T 8077–2012[56]. The maximum diameter in two directions perpendicular to each other were measured by calipers, and the average value was taken as fluidity.
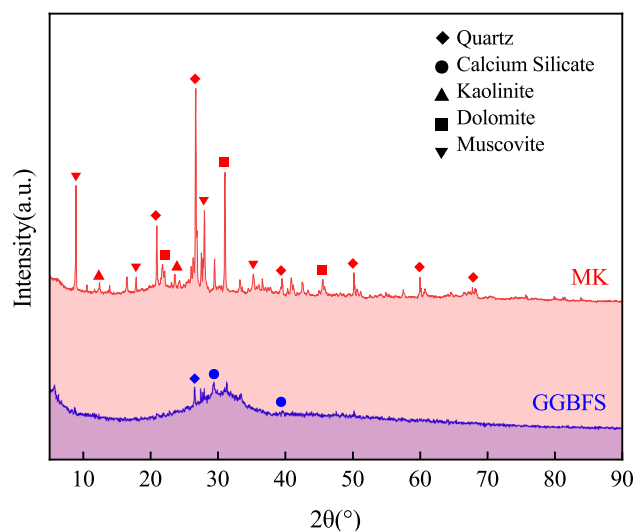
**Figure 3.** XRD patterns of MK and GGBFS.

| Factors | Code | Level | | | | |
|---------|------|-------|------|-----|-----|-------|
| | | −1.414 | −1 | 0 | 1 | 1.414 |
| L/S | $x_1$ | 0.66 | 0.7 | 0.8 | 0.9 | 0.94 |
| Ms | $x_2$ | 1.08 | 1.2 | 1.5 | 1.8 | 1.92 |

**Table 2.** Codes and levels of factors for CCD.

*Compressive strength*
The compressive strength on $40 \times 40 \times 40$ mm hardened paste cubes was tested per Chinese Standard GB/T 17,671–2021, which was the average of 3 samples for each group[57].

*SEM and XRD*
The microstructure and hydration products of samples were characterized by SEM and XRD, respectively. All samples to be measured were soaked in absolute ethanol immediately for 72 h to stop hydration, and placed in an electric thermostatic drying oven for drying. The powdered samples used in XRD were ground after drying and passed through a sieve of 0.075 mm, then packed for testing. The parameters of the XRD were as follows: copper target, 30 kV, 5–90°, 5°/min.

## Experimental results analysis

*Influence of L/S and Ms on workability*
The effects of L/S and Ms were clarified on setting time and fluidity in Fig. 4. It was obvious that the fluidity was significantly improved as L/S increased, while the impact of Ms on fluidity was not such clear. For the setting time, it kept an increasing trend with the increase of L/S. In contrast, when Ms increased, the setting time became shorter. Obviously, all MSGP had higher fluidity than OPC pastes.

Since the activator concentration was 37%, MSGP with L/S of 0.8 had the same water content as OPC pastes with w/b of 0.5. For comparison, when L/S = 0.8, Ms = 1.2, 1.5, 1.8, the fluidities were 212, 226, and 234 mm, respectively, which were 15.8%, 23.5%, and 27.9% higher than that of OPC pastes (183 mm). This was because sodium silicate acted not only as a solvent, but also as a gel. From the perspective of microstructure, it could be considered that sodium silicate was a dispersion of amorphous silicate colloids in an alkaline aqueous medium[58]. Therefore, the interaction between MK and GGBFS particles weakened and improved the fluidity of the fresh pastes. For MK, its tabular granular and clay structure led to higher water demand. The incorporation of GGBFS reduced the amount of MK, so it improved the fluidity of MSGP when the water consumption was fixed. With the increase of Ms, the fluidity of MSGP increased, and the fluidity of Ms = 1.8 was increased by 4.6–12.9% compared to Ms = 1.2 under the same L/S. The reason was the formation of independent silicate micelles in solution at high modulus (< 2.5) helped to disperse precursors particles and improve the rheological properties of the pastes[59].

On the other hand, it was noted that L/S and Ms had an opposite effect on the setting time. In Fig. 4, as L/S increased, the setting time of MSGP prolonged. The time required for the paste to lose fluidity was related to its kinetics. The concentration of active ingredients in the dissolved medium decreased when the water content was high, hence the time required to convert free water to bound water increased accordingly[5]. However, the increase of Ms played an accelerated role in setting. When Ms was 1.2, the initial setting time of MSGP was about
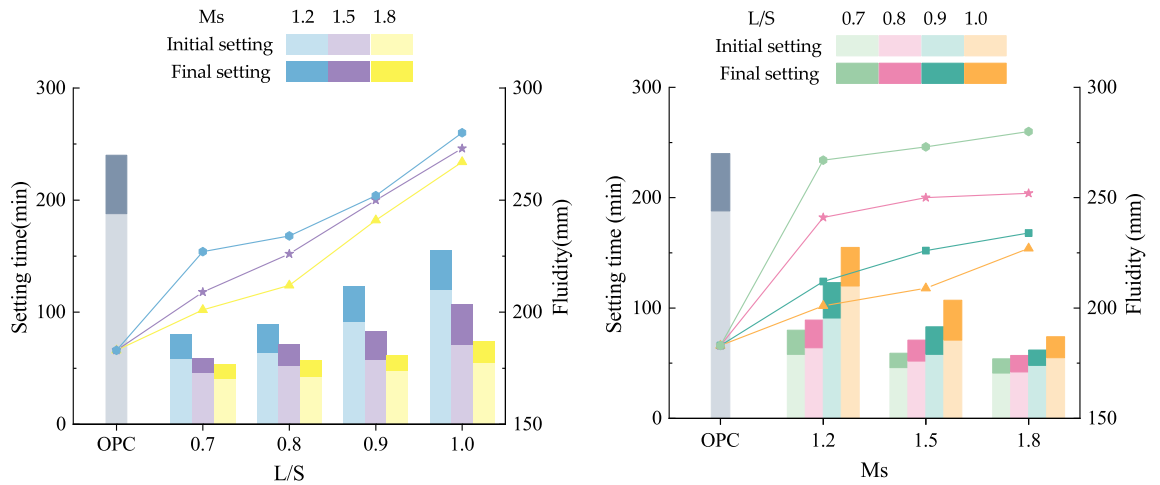
**Figure 4.** Influence of L/S and Ms on workability.

58–120 min, while the initial setting time of MSGP was greatly shortened to 41–55 min after Ms was increased to 1.8. Therefore, the high Ms would shorten the setting time of MSGP. The reason for the shortened setting time is mainly related to $Ca^{2+}$ as charge-balanced ions[60,61]. $Ca^{2+}$ has a stronger charge attraction and neutralization, so the formation of aluminosilicate gels will be faster. At the same time, the presence of $Ca^{2+}$ will cause heterogeneous nucleation effect in the initial reaction process of geopolymers[62]. Heterogeneous nucleation effect also accelerate the formation of geopolymer gels, resulting in a shorter setting time.

*Influence of L/S and Ms on UCS and mass loss*
It was illustrated in Fig. 5 that the comparison of UCS and mass loss changes of each group under different L/S and Ms. The experimental results found that when Ms was constant, the UCS of MSGP decreased with the increase of L/S. When Ms was 1.2, with L/S increased from 0.7 to 1.0, the 28-d UCS were 69.3, 60.8, 59.5, and 46.6 MPa, which were higher than OPC pastes (45.0 MPa). While they were 36.3, 32.0, 31.3, and 27.0 MPa when Ms was 1.8, which were lower than OPC pastes. The UCS of each group was closer to OPC pastes when Ms was 1.5. In summary, the increase of L/S was not conducive to the hardening performance of MSGP, similar to the influence of w/b on the UCS of OPC pastes. According to Davisovits and Heah et al., the fluid medium is more than
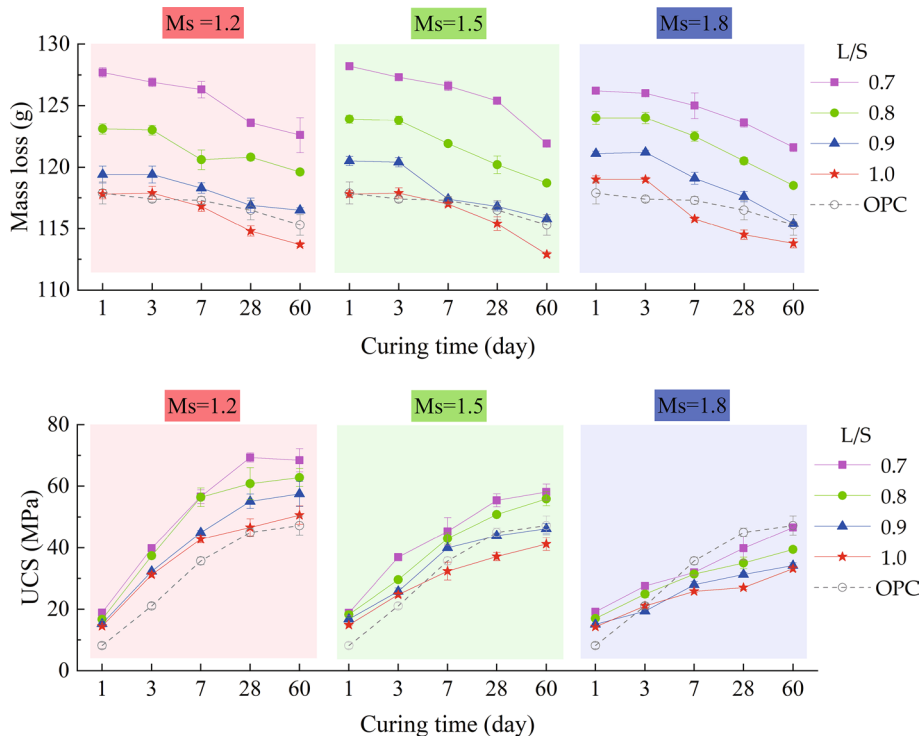


**Figure 5.** Influence of Ms and L/S on UCS and mass loss.

the solid in the mix when L/S is high[31,63]. The contact distance between the activating solution and the precursors is far and limited because of the large volume of the fluid medium, and the dissolution of the aluminosilicate precursor is slow. Instead, when lower L/S is employed, the contact distance between the activating solution and the precursors is improved and the UCS is enhanced as a result.

However, unlike pure water, activators were usually mixed solutions consisting of alkali, soluble silicon, and water, which greatly affected the driving forces of hydration. From Fig. 5, it can be found that when Ms increased from 1.2 to 1.5, the UCS of each group decreased significantly. When L/S was 0.8, The 28-d UCS of the three groups was 60.8, 50.8, and 32.0 MPa, respectively. Especially in the process of Ms increased from 1.5 to 1.8, the UCS decreased more obviously. It was observed that the variation of the UCS (curing time > 28 day) of the three groups of MSGP with different Ms was various. When Ms was 1.2, the 60-d UCS was 68.4, 62.8, 60.6, and 53.2 MPa, which decreased by 1.3% and increased by 3.3%, 1.8%, and 14.2% compared with the 28-d UCS respectively. The increase of UCS was not obvious. While Ms was 1.5, the 60-d UCS was 60.1, 54.2, 51.2, and 44.2 MPa, which increased by 8.5%, 6.7%, 16.6%, and 19.1%. The 60-d UCS increased most when Ms increased to 1.8, which was 22.9%, 23.1%, 14.1%, and 23.0%, respectively, reaching 44.6, 39.4, 35.7, and 33.2 MPa.

It is not difficult to see that the high Ms played a more critical role in the late-age strength development, which was due to the difference in the composition of the activators. For the main components of the modified activator ($Na_2SiO_3$, NaOH), NaOH provides higher solution alkalinity, and the solubility of aluminosilicate is greater under strong alkaline environment, which promotes the polymerization reaction and improves the mechanical properties. When preparing high-modulus sodium silicate solution, it requires less NaOH and leads lower $Na_2O$ content, which inhibits the interactions between active substances and weakening the development of mechanical properties[64]. For the MK-GGBFS system, the high reactivity of GGBFS improves the early reaction of MK-based geopolymers. Increasing Ms within a certain range (it is pointed out that Ms < 2.0[65]) can improve the strength development at 28 days or longer.

## Results and discussion
### Results of CCD method
A total of 13 random mix design tests were performed (include 5 center-point repeat tests) based on the CCD method of the Design-expert software. The mix design and responses are shown in Table 3. The code for the factor 1 L/S is $x_1$, the code for the factor 2 Ms is $x_2$. Response 1 is fluidity (mm), response 2 is initial setting time (min), and response 3, 4, 5, 6 is 3-d, 7-d, 28-d, and 60-d UCS (MPa), respectively.

### Response surface model fitting and verification
Regression fitting analysis was conducted with the experimental data in Table 4. The fitting functions are shown as follows:

$$Fluidity = 225.6 + 22.98x_1 + 13.08x_2 - 3.75x_1x_2 + 2.45x_1^2$$
$$- 1.55x_2^2 - 3.83x_1^2x_2 - 6.73x_1x_2^2 + 3.75x_1^2x_2^2 \tag{1}$$

$$Initial\ setting\ time = 54.6 + 9.9x_1 - 10.96x_2 - 6.5x_1x_2 + 1.20x_1^2$$
$$- 0.55x_2^2 - 4.04x_1^2x_2 + 0.1005x_1x_2^2 + 4.25x_1^2x_2^2 \tag{2}$$

| No | $x_1$ | $x_2$ | Fluidity (mm) | Initial setting time (min) | UCS (MPa) | | | |
|---|---|---|---|---|---|---|---|---|
| | | | | | 3-d | 7-d | 28-d | 60-d |
| 1 | 0.9 | 1.2 | 241 | 91 | 32.3 | 44.9 | 55.1 | 57.5 |
| 2 | 0.8 | 1.5 | 226 | 52 | 29.6 | 43.0 | 50.8 | 54.2 |
| 3 | 0.8 | 1.5 | 221 | 59 | 31.0 | 41.7 | 50.3 | 54.7 |
| 4 | 0.8 | 1.07 | 204 | 69 | 43.3 | 57.9 | 62.1 | 64.5 |
| 5 | 0.94 | 1.5 | 263 | 71 | 24.9 | 33.7 | 39.1 | 45.8 |
| 6 | 0.7 | 1.8 | 227 | 41 | 27.6 | 32.0 | 39.8 | 46.6 |
| 7 | 0.65 | 1.5 | 198 | 43 | 43.5 | 48.1 | 56.9 | 62.2 |
| 8 | 0.8 | 1.5 | 229 | 54 | 29.9 | 43.5 | 50.3 | 54.5 |
| 9 | 0.8 | 1.92 | 241 | 38 | 23.5 | 30.4 | 31.1 | 38.6 |
| 10 | 0.9 | 1.8 | 252 | 48 | 19.4 | 28.0 | 31.3 | 34.2 |
| 11 | 0.8 | 1.5 | 227 | 57 | 32.5 | 43.9 | 53.1 | 56.3 |
| 12 | 0.8 | 1.5 | 225 | 51 | 29.3 | 42.9 | 51.1 | 54.4 |
| 13 | 0.7 | 1.2 | 201 | 58 | 39.8 | 56.6 | 69.3 | 68.4 |

**Table 3.** CCD scheme and experimental results.

| Response | Fluidity | Initial setting time | 3-d UCS | 7-d UCS | 28-d UCS | 60-d UCS |
|---|---|---|---|---|---|---|
| Standard deviation | 2.97 | 3.36 | 1.31 | 0.8307 | 1.16 | 0.8468 |
| C.V.(%) | 1.31 | 5.97 | 4.18 | 1.98 | 2.35 | 1.59 |
| $R^2$ | 0.9920 | 0.9816 | 0.9892 | 0.9973 | 0.9965 | 0.9975 |
| Adj. $R^2$ | 0.9760 | 0.9449 | 0.9676 | 0.9919 | 0.9895 | 0.9925 |
| Adeq precision | 26.3343 | 18.9490 | 22.1304 | 43.2611 | 39.6312 | 48.5419 |
| F-value | 62.04 | 26.70 | 45.73 | 184.06 | 141.70 | 199.41 |
| $p$-value | 0.0006 | 0.0033 | 0.0011 | <0.0001 | 0.0001 | <0.0001 |
| Significance | Yes | Yes | Yes | Yes | Yes | Yes |

**Table 4.** Model validation for the responses.

$$3\text{ - d UCS} = 30.46 - 6.58x_1 - 7x_2 - 0.175x_1x_2 + 1.87x_1^2 \\ + 1.47x_2^2 + 0.7254x_1^2x_2 + 2.65x_1x_2^2 - 4.02x_1^2x_2^2 \tag{3}$$

$$7\text{ - d UCS} = 43 - 5.09x_1 - 9.72x_2 + 1.93x_1x_2 - 1.05x_1^2 + 0.575x_2^2 \\ - 0.6523x_1^2x_2 + 1.17x_1x_2^2 - 2.15x_1^2x_2^2 \tag{4}$$

$$28\text{ - d UCS} = 51.12 - 6.29x_1 - 10.96x_2 + 1.43x_1x_2 - 1.56x_1^2 \\ - 2.26x_2^2 - 2.36x_1^2x_2 + 0.6183x_1x_2^2 + 1.57x_1^2x_2^2 \tag{5}$$

$$60\text{ - d UCS} = 54.82 - 5.8x_1 - 9.16x_2 - 0.375x_1x_2 - 0.41x_1^2 \\ - 1.63x_2^2 - 2.12x_1^2x_2 - 0.0267x_1x_2^2 - 1.1x_1^2x_2^2 \tag{6}$$

Model validation was performed on the above response surface functions, and the results are shown in Table 4.

Table 4 showed that the $p$-values of the regression models of the fluidity, initial setting time, and UCS (3-d, 7-d, 28-d, 60-d) were all < 0.01, indicating that these six mathematical models were statistically significant. The $R^2$ of the fitting equations were 0.9920, 0.9816, 0.9892, 0.9973, 0.9965, and 0.9975, respectively, which indicated that the six statistical models could explain the changes in response values of 99.20%, 98.16%, 98.92%, 99.73%, 99.65%, and 99.75%. It informed that the predicted values agree with the actual results approximately and the experimental error was not obvious. In addition, the C.V. of the models were all less than 10%, which showed that the experiment had high reliability and precision. The adequate precision greater than 4 could be considered as desirable, and all the equations above are satisfied. Figure 6 illustrates the relationships between the predicted values and the experimental values.

## ANOVA and interaction

The ANOVA of the models of the fluidity, initial setting time, UCS (3-d, 7-d, 28-d, 60-d) are shown in Tables 5–7. From the statistical hypothesis testing, if the $p$-value $\leq 0.05$, this factor is considered to have a significant effect on the response value, and vice versa[66]. The $p$-values of the above six regression equations were all less than 0.01, it could be considered that the fitting of the model is statistically significant. While the $p$-values of the lack of fit of each equation were greater than 0.05, there was a tiny discrepancy between the model and the experimental results. That was, the model fitted well. For the factor interactions under each response value, the $p$-value of each item was greater than 0.05, which had almost no effect on the response values.

According to the regression models, as shown in Fig. 7, the 3D response surface diagrams of different response values could be obtained. The response values were displayed from purple to red in order of smallest to largest. The contours projected from the response surface to the bottom could be used to reflect the change in the response value, and the denser the contours were, the faster the response values changed, then the greater the influence of the factors were. It can be seen from Fig. 7 that the interactions of factors in the design interval were weak, and the maximum value point did not appear in the single response surface. There was a constraint relationship between the response values. For example, the increase of L/S had a positive effect on the fluidity, but it prolonged the setting time and reduced the mechanical properties. The reduction of Ms was beneficial to the mechanical properties, but it affected the workability of the paste and made it difficult to stir and form. These showed that the influence of L/S and Ms on the fluidity, setting time, and compressive strength in the selected interval needed to be considered comprehensively, not for one certain response value.

## Optimum mix of MSGP based on CCD method

Just as mentioned above, for anisotropic concrete materials, a single response value was not an optimization goal of its performance, but should comprehensively considered the workability, mechanical property and other performances. According to the actual condition, the target fluidity is 220 mm, and the initial setting time is between 30 and 50 min considering the quick setting of GGBFS, then the optimum mix ratio based on the maximum 28-d
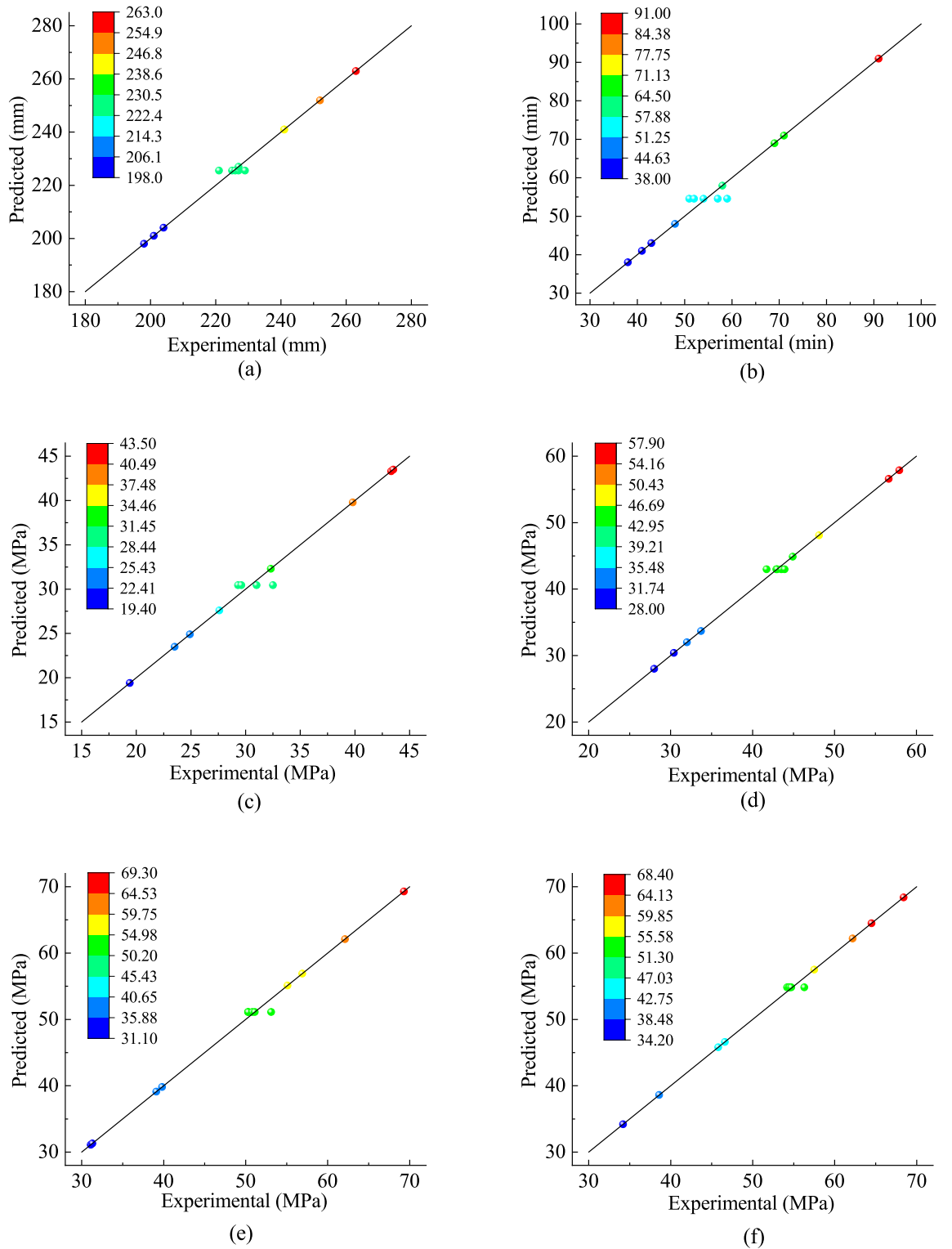
**Figure 6.** Comparison of predicted and experimental values:(**a**) Fluidity; (**b**) Initial setting time; (**c**) 3-d UCS; (**d**) 7-d UCS; (**e**) 28-d UCS; and (**f**) 60-d UCS.

UCS is: L/S = 0.75, Ms = 1.55. Under the same test conditions, the MSGP was produced with the optimum mix ratio. The measured fluidity was 216 mm, the initial setting time was 53 min, and the 28-d UCS was 53.10 MPa. Table 8 compares the experimental and predicted values of the optimum mix ratio. The mean absolute percentage error (MAPE) of the experimental and predicted values was calculated according to the following formula[67].

| Response | Variation Source | Sum of Squares | df | Mean Square | F-value | p-value |
|---|---|---|---|---|---|---|
| Fluidity | Model | 4367.57 | 8 | 545.95 | 62.04 | 0.0006 |
| | $x_1$ | 2112.50 | 1 | 2112.50 | 240.06 | 0.0001 |
| | $x_2$ | 684.50 | 1 | 684.50 | 77.78 | 0.0009 |
| | $x_1x_2$ | 56.25 | 1 | 56.25 | 6.39 | 0.0648 |
| | $x_1^2$ | 34.30 | 1 | 34.30 | 3.90 | 0.1196 |
| | $x_2^2$ | 13.73 | 1 | 13.73 | 1.56 | 0.2798 |
| | $x_1^2x_2$ | 29.36 | 1 | 29.36 | 3.34 | 0.1418 |
| | $x_1x_2^2$ | 90.61 | 1 | 90.61 | 10.30 | 0.0326 |
| | $x_1^2x_2^2$ | 28.13 | 1 | 28.13 | 3.20 | 0.1483 |
| | Residual | 327.24 | 10 | 32.72 | | |
| | Lack of Fit | 292.04 | 6 | 48.67 | 5.53 | 0.0599 |
| | Pure Error | 35.20 | 4 | 8.80 | | |
| | Cor Total | 4402.77 | 12 | | | |

**Table 5.** ANOVA of regression model.

| Response | Variation Source | Sum of Squares | df | Mean Square | F-value | p-value |
|---|---|---|---|---|---|---|
| Initial setting time | Model | 2413.57 | 8 | 301.70 | 26.70 | 0.0033 |
| | $x_1$ | 392.00 | 1 | 392.00 | 34.69 | 0.0042 |
| | $x_2$ | 480.50 | 1 | 480.50 | 42.52 | 0.0029 |
| | $x_1x_2$ | 169.00 | 1 | 169.00 | 14.96 | 0.0180 |
| | $x_1^2$ | 8.23 | 1 | 8.23 | 0.7282 | 0.4416 |
| | $x_2^2$ | 1.73 | 1 | 1.73 | 0.1530 | 0.7157 |
| | $x_1^2x_2$ | 32.64 | 1 | 32.64 | 2.89 | 0.1644 |
| | $x_1x_2^2$ | 0.0202 | 1 | 0.0202 | 0.0018 | 0.9683 |
| | $x_1^2x_2^2$ | 36.13 | 1 | 36.13 | 3.20 | 0.1483 |
| | Residual | 149.93 | 9 | 16.66 | | |
| | Lack of Fit | 104.73 | 5 | 20.95 | 1.85 | 0.2848 |
| | Pure Error | 45.20 | 4 | 11.30 | | |
| | Cor Total | 2458.77 | 12 | | | |

**Table 6.** ANOVA of initial setting time regression model.

$$\text{MAPE (\% )} = \frac{\text{Experimental - Predicted}}{\text{Experimental}} \times 100\% \tag{7}$$

## Microstructural analysis

In order to further study the effects of L/S and Ms on the polymerization reaction, workability, and mechanical properties of MSGP, the microstructure was determined by XRD-SEM method. It was explained from two aspects: hydration reaction products and micropore changes.

## XRD

Figure 8 shows the XRD patterns of MSGP after curing for 7 and 28 days. In the initial hydration, the formation of quartz ($SiO_2$), mullite ($3Al_2O_3·2SiO_2$), kaolinite ($Al_2Si_2O_5(OH)_4$), calcite ($CaCO_3$), etc., as well as the diffuse peak of C–A–S–H (around $2\theta = 30°$), could be observed. The phase of kaolinite is attributed to the unreacted metakaolin[68]. The presence of calcite is due to the fact that, ambient $CO_2$ reacted with during the polymerization reaction[69]. The $Ca(OH)_2$ is generated by the reaction between $Ca^{2+}$ dissolved in the MSGP samples and $OH^-$ in the alkali solution. As hydration continued, the tobermorite (($CaO)_x$–$SiO_2$–$zH_2O$) began to be observed in the spectrum[70]. At the same time, it was found that the formation of C–A–S–H gel and its nearby aragonite and calcite increased. The dissolved alumina in the precursors react with $OH^-$ in the alkali solution and form tetrahedral $[H_3AlO_4]^-$ and octahedral $[Al(OH)_6]^{3-}$. Then $[H_3AlO_4]^-$ further reacts with $Ca^{2+}$ to form C–A–S–H gel[49,71,72]. L/S and Ms did not affect the phase of the hydration products too much, and then they had little effect on the final hydration products. However, it promoted the polymerization reaction of the paste because the dissolution rate of the aluminosilicate precursor changed.

| Response | Variation Source | Sum of Squares | df | Mean Square | F-value | p-value |
|---|---|---|---|---|---|---|
| 3-d UCS | Model | 626.71 | 8 | 78.34 | 45.73 | 0.0011 |
| | $x_1$ | 172.98 | 1 | 172.98 | 100.98 | 0.0006 |
| | $x_2$ | 196.02 | 1 | 196.02 | 114.43 | 0.0004 |
| | $x_1x_2$ | 0.1225 | 1 | 0.1225 | 0.0715 | 0.8024 |
| | $x_1^2$ | 19.98 | 1 | 19.98 | 11.67 | 0.0269 |
| | $x_2^2$ | 12.35 | 1 | 12.35 | 7.21 | 0.0550 |
| | $x_1^2x_2$ | 1.05 | 1 | 1.05 | 0.6143 | 0.4770 |
| | $x_1x_2^2$ | 14.06 | 1 | 14.06 | 8.21 | 0.0457 |
| | $x_1x_2^2$ | 32.40 | 1 | 32.40 | 18.91 | 0.0122 |
| | Residual | 60.55 | 10 | 6.05 | | |
| | Lack of Fit | 53.69 | 6 | 8.95 | 5.22 | 0.0657 |
| | Pure Error | 6.85 | 4 | 1.71 | | |
| | Cor Total | 633.56 | 12 | | | |
| 7-d UCS | Model | 1016.01 | 8 | 127.00 | 184.06 | <0.0001 |
| | $x_1$ | 103.68 | 1 | 103.68 | 150.26 | 0.0003 |
| | $x_2$ | 378.13 | 1 | 378.13 | 548.01 | <0.0001 |
| | $x_1x_2$ | 14.82 | 1 | 14.82 | 21.48 | 0.0098 |
| | $x_1^2$ | 6.30 | 1 | 6.30 | 9.13 | 0.0391 |
| | $x_2^2$ | 1.89 | 1 | 1.89 | 2.74 | 0.1733 |
| | $x_1^2x_2$ | 0.8509 | 1 | 0.8509 | 1.23 | 0.3290 |
| | $x_1x_2^2$ | 2.72 | 1 | 2.72 | 3.94 | 0.1181 |
| | $x_1^2x_2^2$ | 9.24 | 1 | 9.24 | 13.40 | 0.0216 |
| | Residual | 15.58 | 7 | 2.23 | | |
| | Lack of Fit | 12.82 | 3 | 4.27 | 6.19 | 0.0553 |
| | Pure Error | 2.76 | 4 | 0.6900 | | |
| | Cor Total | 1018.77 | 12 | | | |
| 28-d UCS | Model | 1521.30 | 8 | 190.16 | 141.70 | 0.0001 |
| | $x_1$ | 158.42 | 1 | 158.42 | 118.05 | 0.0004 |
| | $x_2$ | 480.50 | 1 | 480.50 | 358.05 | <0.0001 |
| | $x_1x_2$ | 8.12 | 1 | 8.12 | 6.05 | 0.0697 |
| | $x_1^2$ | 13.91 | 1 | 13.91 | 10.36 | 0.0323 |
| | $x_2^2$ | 29.19 | 1 | 29.19 | 21.75 | 0.0096 |
| | $x_1^2x_2$ | 11.18 | 1 | 11.18 | 8.33 | 0.0447 |
| | $x_1x_2^2$ | 0.7645 | 1 | 0.7645 | 0.5696 | 0.4924 |
| | $x_1^2x_2^2$ | 4.96 | 1 | 4.96 | 3.70 | 0.1269 |
| | Residual | 22.28 | 7 | 3.18 | | |
| | Lack of Fit | 16.91 | 3 | 5.64 | 4.20 | 0.0997 |
| | Pure Error | 5.37 | 4 | 1.34 | | |
| | Cor Total | 1526.67 | 12 | | | |
| 60-d UCS | Model | 1143.82 | 8 | 142.98 | 199.41 | <0.0001 |
| | $x_1$ | 134.48 | 1 | 134.48 | 187.56 | 0.0002 |
| | $x_2$ | 335.40 | 1 | 335.40 | 467.79 | <0.0001 |
| | $x_1x_2$ | 0.5625 | 1 | 0.5625 | 0.7845 | 0.4258 |
| | $x_1^2$ | 0.9606 | 1 | 0.9606 | 1.34 | 0.3115 |
| | $x_2^2$ | 15.28 | 1 | 15.28 | 21.30 | 0.0099 |
| | $x_1^2x_2$ | 8.97 | 1 | 8.97 | 12.51 | 0.0241 |
| | $x_1x_2^2$ | 0.0014 | 1 | 0.0014 | 0.0020 | 0.9665 |
| | $x_1^2x_2^2$ | 2.42 | 1 | 2.42 | 3.38 | 0.1401 |
| | Residual | 14.26 | 7 | 2.04 | | |
| | Lack of Fit | 11.39 | 3 | 3.80 | 5.30 | 0.0705 |
| | Pure Error | 2.87 | 4 | 0.7170 | | |
| | Cor Total | 1146.68 | 12 | | | |

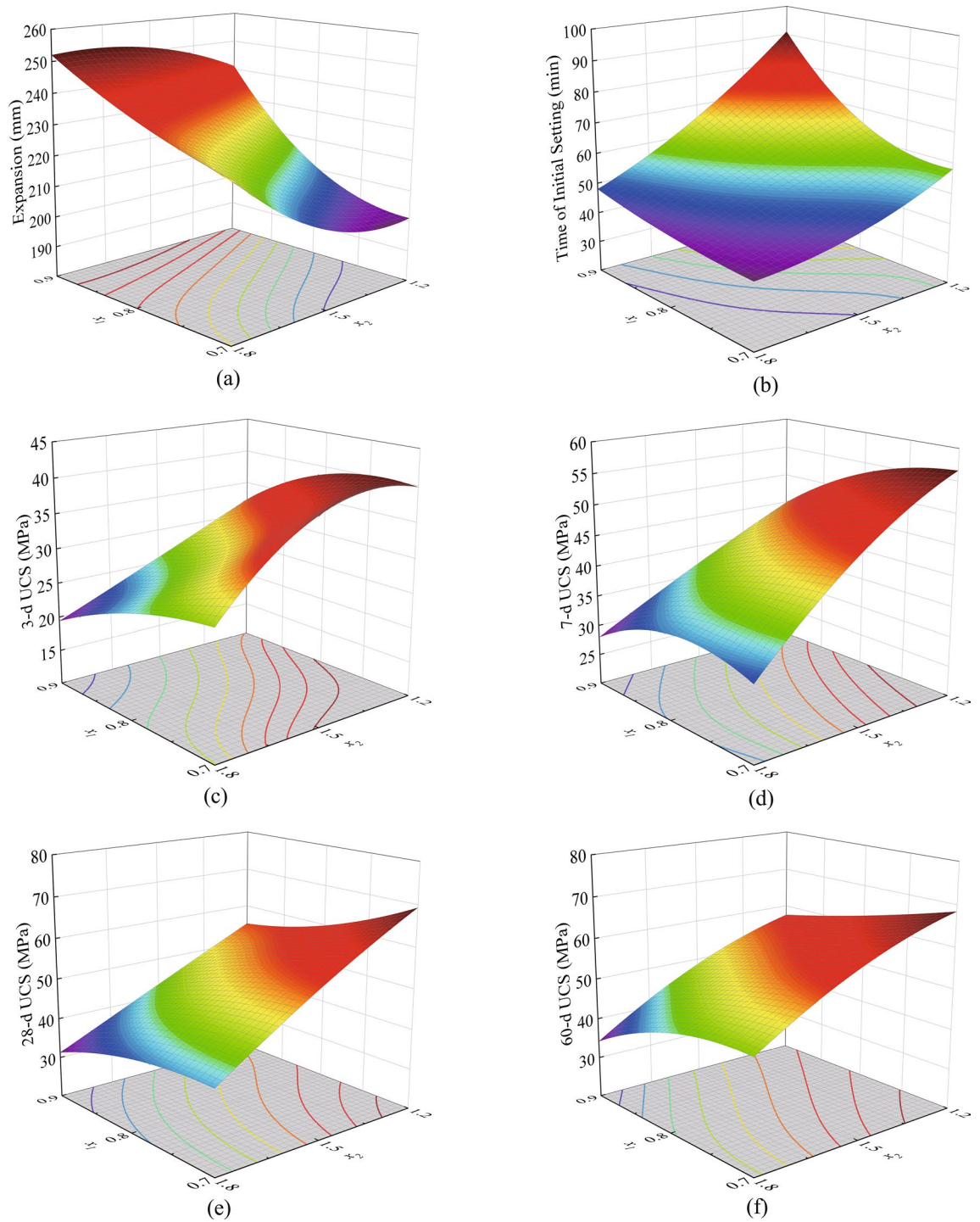**Table 7.** ANOVA of the UCS regression model.

**Figure 7.** 3D response surface diagrams for the effects of L/S and Ms on (**a**) Fluidity; (**b**) Initial setting time; (**c**) 3-d UCS; (**d**) 7-d UCS; (**e**) 28-d UCS; and (**f**) 60-d UCS.

| Term | Units | Experimental | Predicted | MAPE (%) |
|---|---|---|---|---|
| Fluidity | mm | 216 | 220 | − 1.81 |
| Initial setting time | min | 53 | 50 | 6.00 |
| 28-d UCS | MPa | 53.10 | 51.36 | 3.28 |

**Table 8.** Comparison between the experimental and predicted values of the optimized mix.
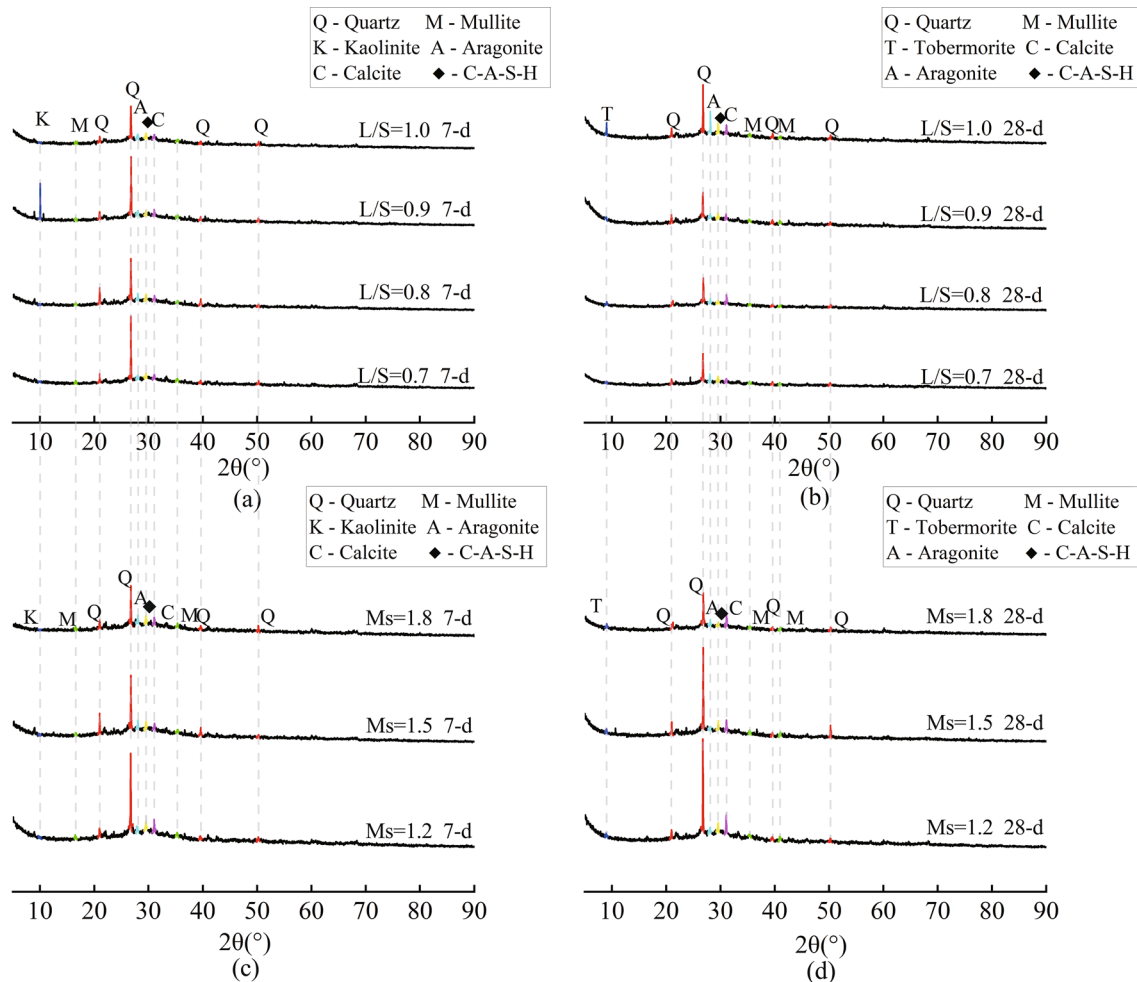
**Figure 8.** XRD patterns of MSGP: (**a**) Ms = 1.5, 7-d; (**b**) Ms = 1.5, 28-d; (**c**) L/S = 0.8, 7-d; (**d**) L/S = 0.8, 28-d.

### SEM

The SEM diagrams of 28-d MSGP are shown in Fig. 9. It could be seen from the diagram that for MSGP with constant Ms, the increase of L/S had an adverse effect on the compactness of the gel structure. It was reflected in the microstructure with the rough and porous gel morphology and the further increase of the width of the microcracks. The mechanical properties of MSGP worsened due to the presence of pores and cracks [69]. This is consistent with the above results of experiments. On the other hand, the increase of Ms improved the workability of MSGP. The frictional resistance between the particles was reduced due to the action of the sodium silicate micelle. However, the rapid polymerization reaction was not conducive to the binding of low active ingredients, which appeared porous and disordered from a micro view, then reducing the macroscopic mechanical properties.

### Conclusions

In this research, the impacts of liquid–solid ratio (L/S) and modulus of sodium silicate (Ms) on the workability and mechanical performances of MK-GGBFS based geopolymer paste (MSGP) were investigated. Then, the optimum mix ratio was found using the central composite design method for all the three properties simultaneously. The main conclusions are listed below:

(1) The synergy between metakaolin (MK) and ground granulated blast furnace slag (GGBFS) is good. The setting time can be extended effectively by partially replacing GGBFS with MK, overcoming the defect of quick harden of GGBFS-based geopolymer.

(2) When L/S was raised from 0.7 to 1, the workability was effectively improved. When Ms was 1.5, the fluidity increased from 209 to 273 mm, and the initial setting time prolonged from 46 to 71 min. With the increasement of Ms from 1.2 to 1.8, the fluidity increased from 201 to 227 mm when L/S was 0.7, but the initial setting time shortened slightly from 58 to 41 min.

(3) The regression models established by central composite design method fitted well on the six response values, and the $R^2$ were all above 0.98. The optimum mix ratio with L/S ratio of 0.75 and Ms value of 1.55 was obtained. The measured fluid is 216 mm, the initial setting time is 53 min, and the 28-d unconfined compressive strength is 53.1 MPa.
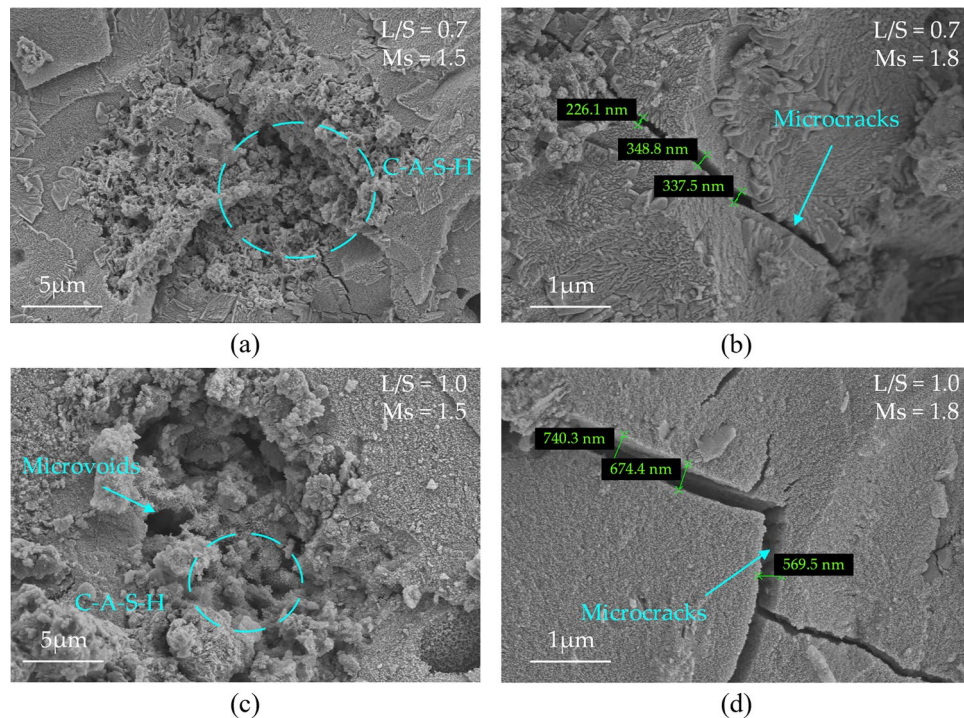
**Figure 9.** 28-d SEM diagram of four mix proportion: (**a**) L/S = 0.7, Ms = 1.5; (**b**) L/S = 0.7, Ms = 1.8; (**c**) L/S = 1.0, Ms = 1.5; (**d**) L/S = 1.0, Ms = 1.8.

## Data availability

All data generated or analyzed during this study are included in this published article.

## References

1. Industrial Solid Waste. http://www.chinagygfw.com/.
2. Castro-Pardo, S. *et al.* A comprehensive overview of carbon dioxide capture: From materials, methods to industrial status. *Mater. Today* **60**, 227–270. https://doi.org/10.1016/j.mattod.2022.08.018 (2022).
3. | Greenhouse Gas (GHG) Emissions|Climate Watch. https://www.climatewatchdata.org/ghg-emissions?end_year=2020&start_year=1990.
4. Zhang, Q. *et al.* Utilization of solid wastes to sequestrate carbon dioxide in cement-based materials and methods to improve carbonation degree: A review. *J CO2 Util* **72**, 102502. https://doi.org/10.1016/j.jcou.2023.102502 (2023).
5. Xie, T., Visintin, P., Zhao, X. & Gravina, R. Mix design and mechanical properties of geopolymer and alkali activated concrete: Review of the state-of-the-art and the development of a new unified approach. *Constr. Build. Mater.* **256**, 119380. https://doi.org/10.1016/j.conbuildmat.2020.119380 (2020).
6. Bai, T., Song, Z., Wang, H., Wu, Y. & Huang, W. Performance evaluation of metakaolin geopolymer modified by different solid wastes. *J. Clean. Prod.* **226**, 114–121. https://doi.org/10.1016/j.jclepro.2019.04.093 (2019).
7. Zhang, P. *et al.* Properties of fresh and hardened fly ash/slag based geopolymer concrete: A review. *J. Clean. Prod.* **270**, 122389. https://doi.org/10.1016/j.jclepro.2020.122389 (2020).
8. Hadi, M. N. S., Zhang, H. & Parkinson, S. Optimum mix design of geopolymer pastes and concretes cured in ambient condition based on compressive strength, setting time and workability. *J. Build. Eng.* **23**, 301–313. https://doi.org/10.1016/j.jobe.2019.02.006 (2019).
9. Shi, C., Qu, B. & Provis, J. L. Recent progress in low-carbon binders. *Cem. Concr. Res.* **122**, 227–250. https://doi.org/10.1016/j.cemconres.2019.05.009 (2019).
10. John, S. K., Nadir, Y. & Girija, K. Effect of source materials, additives on the mechanical properties and durability of fly ash and fly ash-slag geopolymer mortar: A review. *Constr. Build. Mater.* **280**, 122443. https://doi.org/10.1016/j.conbuildmat.2021.122443 (2021).
11. Valencia-Saavedra, W. G., Mejía De Gutiérrez, R. & Puertas, F. Performance of FA-based geopolymer concretes exposed to acetic and sulfuric acids. *Constr. Build. Mater.* **257**, 119503. https://doi.org/10.1016/j.conbuildmat.2020.119503 (2020).
12. Nodehi, M., Ozbakkaloglu, T., Gholampour, A., Mohammed, T. & Shi, X. The effect of curing regimes on physico-mechanical, microstructural and durability properties of alkali-activated materials: A review. *Constr. Build. Mater.* **321**, 126335. https://doi.org/10.1016/j.conbuildmat.2022.126335 (2022).
13. Wang, Y.-S., Peng, K.-D., Alrefaei, Y. & Dai, J.-G. The bond between geopolymer repair mortars and OPC concrete substrate: Strength and microscopic interactions. *Cem. Concr. Compos.* **119**, 103991. https://doi.org/10.1016/j.cemconcomp.2021.103991 (2021).
14. Martínez, A. & Miller, S. A. A review of drivers for implementing geopolymers in construction: Codes and constructability. *Resour. Conserv. Recycl.* **199**, 107238. https://doi.org/10.1016/j.resconrec.2023.107238 (2023).
15. Provis, J. & Van Deventer, J. *Geopolymers: Structures, Processing Properties and Industrial Applications* (Elsevier, 2009).

16. Alrefaei, Y. & Dai, J.-G. Tensile behavior and microstructure of hybrid fiber ambient cured one-part engineered geopolymer composites. *Constr. Build. Mater.* **184**, 419–431. https://doi.org/10.1016/j.conbuildmat.2018.07.012 (2018).

17. Rajan, H. S. & Kathirvel, P. Sustainable development of geopolymer binder using sodium silicate synthesized from agricultural waste. *J. Clean. Prod.* **286**, 124959. https://doi.org/10.1016/j.jclepro.2020.124959 (2021).

18. Fang, S., Lam, E. S. S., Li, B. & Wu, B. Effect of alkali contents, moduli and curing time on engineering properties of alkali activated slag. *Constr. Build. Mater.* **249**, 118799. https://doi.org/10.1016/j.conbuildmat.2020.118799 (2020).

19. Nedeljković, M., Li, Z. & Ye, G. Setting, Strength, and Autogenous Shrinkage of Alkali-Activated Fly Ash and Slag Pastes: Effect of Slag Content. *Materials* **11**, 2121. https://doi.org/10.3390/ma11112121 (2018).

20. Puertas, F. *et al.* Alkali-activated slag concrete: Fresh and hardened behaviour. *Cem. Concr. Compos.* **85**, 22–31. https://doi.org/10.1016/j.cemconcomp.2017.10.003 (2018).

21. Alventosa, K. M. L. & White, C. E. The effects of calcium hydroxide and activator chemistry on alkali-activated metakaolin pastes. *Cem. Concr. Res.* **145**, 106453. https://doi.org/10.1016/j.cemconres.2021.106453 (2021).

22. Chen, L., Wang, Z., Wang, Y. & Feng, J. Preparation and Properties of Alkali Activated Metakaolin-Based Geopolymer. *Materials* **9**, 767. https://doi.org/10.3390/ma9090767 (2016).

23. Li, Z., Liang, X., Chen, Y. & Ye, G. Effect of metakaolin on the autogenous shrinkage of alkali-activated slag-fly ash paste. *Constr. Build. Mater.* **278**, 122397. https://doi.org/10.1016/j.conbuildmat.2021.122397 (2021).

24. Li, Z., Nedeljković, M., Chen, B. & Ye, G. Mitigating the autogenous shrinkage of alkali-activated slag by metakaolin. *Cem. Concr. Res.* **122**, 30–41. https://doi.org/10.1016/j.cemconres.2019.04.016 (2019).

25. Bernal, S. A., Provis, J. L., Rose, V. & Mejía De Gutierrez, R. Evolution of binder structure in sodium silicate-activated slag-metakaolin blends. *Cem. Concr. Compos.* **33**, 46–54. https://doi.org/10.1016/j.cemconcomp.2010.09.004 (2011).

26. Alanazi, H., Hu, J. & Kim, Y.-R. Effect of slag, silica fume, and metakaolin on properties and performance of alkali-activated fly ash cured at ambient temperature. *Constr. Build. Mater.* **197**, 747–756. https://doi.org/10.1016/j.conbuildmat.2018.11.172 (2019).

27. Zhang, H. Y., Kodur, V., Wu, B., Cao, L. & Wang, F. Thermal behavior and mechanical properties of geopolymer mortar after exposure to elevated temperatures. *Constr. Build. Mater.* **109**, 17–24. https://doi.org/10.1016/j.conbuildmat.2016.01.043 (2016).

28. Habert, G., d'Espinose De Lacaillerie, J. B. & Roussel, N. An environmental evaluation of geopolymer based concrete production: Reviewing current research trends. *J. Clean. Prod.* **19**, 1229–1238. https://doi.org/10.1016/j.jclepro.2011.03.012 (2011).

29. Danish, A. *et al.* Performance evaluation and cost analysis of prepacked geopolymers containing waste marble powder under different curing temperatures for sustainable built environment. *Resour. Conserv. Recycl.* **192**, 106910. https://doi.org/10.1016/j.resconrec.2023.106910 (2023).

30. Kim, B. *et al.* Effect of Si/Al molar ratio and curing temperatures on the immobilization of radioactive borate waste in metakaolin-based geopolymer waste form. *J. Hazard. Mater.* **458**, 131884. https://doi.org/10.1016/j.jhazmat.2023.131884 (2023).

31. Heah, C. Y. *et al.* Study on solids-to-liquid and alkaline activator ratios on kaolin-based geopolymers. *Constr. Build. Mater.* **35**, 912–922. https://doi.org/10.1016/j.conbuildmat.2012.04.102 (2012).

32. Cheng, H. *et al.* Effect of solid-to-liquid ratios on the properties of waste catalyst–metakaolin based geopolymers. *Constr. Build. Mater.* **88**, 74–83. https://doi.org/10.1016/j.conbuildmat.2015.01.005 (2015).

33. Ranjbar, N., Kashefi, A. & Maheri, M. R. Hot-pressed geopolymer: Dual effects of heat and curing time. *Cem. Concr. Compos.* **86**, 1–8. https://doi.org/10.1016/j.cemconcomp.2017.11.004 (2018).

34. Zhang, H., Ji, Z., Zeng, Y. & Pei, Y. Solidification/stabilization of landfill leachate concentrate contaminants using solid alkali-activated geopolymers with a high liquid solid ratio and fixing rate. *Chemosphere* **288**, 132495. https://doi.org/10.1016/j.chemosphere.2021.132495 (2022).

35. Wang, W., Fan, C., Wang, B., Zhang, X. & Liu, Z. Workability, rheology, and geopolymerization of fly ash geopolymer: Role of alkali content, modulus, and water–binder ratio. *Constr. Build. Mater.* **367**, 130357. https://doi.org/10.1016/j.conbuildmat.2023.130357 (2023).

36. Montgomery, D. C. *Design and Analysis of Experiments* 478–544 (Wiley, 2013).

37. Myers, R. H., Montgomery, D. C. & Anderson, C. *Response surface methodology: process and product optimization using designed experiments* (Wiley, 2016).

38. Thomareis, A. S. & Dimitreli, G. Chapter 12 - Techniques used for processed cheese characterization. In *Processed cheese science and technology* (eds El-Bakry, M. & Mehta, B. M.) 295–349 (Woodhead Publishing, 2022).

39. Ramalingam, B. & Das, S. K. Biofabricated graphene-magnetite nanobioaerogel with antibiofilm property: Response surface methodology based optimization for effective removal of heavy metal ions and killing of bacterial pathogens. *Chem. Eng. J.* **475**, 145976. https://doi.org/10.1016/j.cej.2023.145976 (2023).

40. Yang, F., Feng, H., Wu, L., Zhang, Z. & Wang, J. Performance prediction and parameters optimization of an opposed-piston free piston engine generator using response surface methodology. *Energy Convers. Manag.* **295**, 117633. https://doi.org/10.1016/j.enconman.2023.117633 (2023).

41. Suresh Nair, M., Rajarathinam, R., Velmurugan, S. & Subhani, S. An optimized approach towards bio-capture and carbon dioxide sequestration with microalgae Phormidium valderianum using response surface methodology. *Bioresour. Technol.* **389**, 129838. https://doi.org/10.1016/j.biortech.2023.129838 (2023).

42. Zhao, D., Chen, M., Lv, J., Lei, Z. & Song, W. Multi-objective optimization of battery thermal management system combining response surface analysis and NSGA-II algorithm. *Energy Convers. Manag.* **292**, 117374. https://doi.org/10.1016/j.enconman.2023.117374 (2023).

43. Lu, H., Dong, Q., Yan, S., Chen, X. & Wang, X. Development of flexible grouting material for cement-stabilized macadam base using response surface and genetic algorithm optimization methodologies. *Constr. Build. Mater.* **409**, 133823. https://doi.org/10.1016/j.conbuildmat.2023.133823 (2023).

44. Watson, M. A. *et al.* Response surface methodology investigation into the interactions between arsenic and humic acid in water during the coagulation process. *J. Hazard. Mater.* **312**, 150–158. https://doi.org/10.1016/j.jhazmat.2016.03.002 (2016).

45. Saffron, S. *Science Technology and Health* 139–167 (Woodhead Publishing, 2020). https://doi.org/10.1016/B978-0-12-818638-1.00009-5.

46. Maaze, M. R. & Shrivastava, S. Design optimization of a recycled concrete waste-based brick through alkali activation using Box-Behnken design methodology. *J. Build. Eng.* **75**, 106863. https://doi.org/10.1016/j.jobe.2023.106863 (2023).

47. Rooholghodos, S. H., Pourmadadi, M., Yazdian, F. & Rashedi, H. Optimization of electrospun CQDs-Fe3O4-RE loaded PVA-cellulose nanofibrils via central composite design for wound dressing applications: Kinetics and in vitro release study. *Int. J. Biol. Macromol.* **237**, 124067. https://doi.org/10.1016/j.ijbiomac.2023.124067 (2023).

48. Du, S., Ge, X. & Zhao, Q. Central composite design-based development of eco-efficient high-volume fly ash mortar. *Constr. Build. Mater.* **358**, 129411. https://doi.org/10.1016/j.conbuildmat.2022.129411 (2022).

49. Sun, Z. & Vollpracht, A. Isothermal calorimetry and in-situ XRD study of the NaOH activated fly ash, metakaolin and slag. *Cem. Concr. Res.* **103**, 110–122. https://doi.org/10.1016/j.cemconres.2017.10.004 (2018).

50. Oshani, F., Allahverdi, A., Kargari, A., Norouzbeigi, R. & Mahmoodi, N. M. Effect of preparation parameters on properties of metakaolin-based geopolymer activated by silica fume- sodium hydroxide alkaline blend. *J. Build. Eng.* **60**, 104984. https://doi.org/10.1016/j.jobe.2022.104984 (2022).

51. Jiang, T., Liu, Z., Tian, X., Wu, J. & Wang, L. Review on the impact of metakaolin-based geopolymer's reaction chemistry, nano-structure and factors on its properties. *Constr. Build. Mater.* **412**, 134760. https://doi.org/10.1016/j.conbuildmat.2023.134760 (2024).
52. Gao, K. *et al.* Effects SiO$_2$/Na$_2$O molar ratio on mechanical properties and the microstructure of nano-SiO$_2$ metakaolin-based geopolymers. *Constr. Build. Mater.* **53**, 503–510. https://doi.org/10.1016/j.conbuildmat.2013.12.003 (2014).
53. Zhan, J. *et al.* Effect of Slag on the Strength and Shrinkage Properties of Metakaolin-Based Geopolymers. *Materials* **15**, 2944. https://doi.org/10.3390/ma15082944 (2022).
54. Yang, Z., Shi, P., Zhang, Y. & Li, Z. Influence of liquid-binder ratio on the performance of alkali-activated slag mortar with supera-bsorbent polymer. *J. Build. Eng.* **48**, 103934. https://doi.org/10.1016/j.jobe.2021.103934 (2022).
55. GB/T 1346–2011. Teat method for water requirement of normal consistency, setting time and soundness of Portland cement. 2011.
56. GB/T 8077–2012. Methods for testing uniformity of concrete admixture. 2012.
57. GB/T 17671–2021. Methods for testing uniformity of concrete admixture. 2012.
58. Tognonvi, M. T., Massiot, D., Lecomte, A., Rossignol, S. & Bonnet, J.-P. Identification of solvated species present in concentrated and dilute sodium silicate solutions by combined 29Si NMR and SAXS studies. *J. Colloid Interface Sci.* **352**, 309–315. https://doi.org/10.1016/j.jcis.2010.09.018 (2010).
59. Stempkowska, A., Mastalska-Popławska, J., Izak, P., Ogłaza, L. & Turkowska, M. Stabilization of kaolin clay slurry with sodium silicate of different silicate moduli. *Appl. Clay Sci.* **146**, 147–151. https://doi.org/10.1016/j.clay.2017.05.046 (2017).
60. Cui, C. *et al.* Influence of GGBFS content and activator modulus on curing of metakaolin based geopolymer at ambient temperature. *J. Build. Mater.* **20**, 535–542. https://doi.org/10.3969/j.issn.1007-9629.2017.04.008 (2017).
61. Jia, Y., Han, M., Meng, X. & Xu, Z. Study on setting time of fly ash-based geopolymer. *B. Chin. Ceram. Soc.* **28**, 893–899 (2009).
62. Lee, W. K. W. & Van Deventer, J. S. J. The effect of ionic contaminants on the early-age properties of alkali-activated fly ash-based cements. *Cem. Concr. Res.* **32**, 577–584. https://doi.org/10.1016/S0008-8846(01)00724-4 (2002).
63. Davidovits, J. *Geopolymer: Chemistry & Applications*. (Institut Géopolymère, Saint-Quentin, 2020).
64. Ling, Y., Wang, K., Wang, X. & Hua, S. Effects of mix design parameters on heat of geopolymerization, set time, and compressive strength of high calcium fly ash geopolymer. *Constr. Build. Mater.* **228**, 116763. https://doi.org/10.1016/j.conbuildmat.2019.116763 (2019).
65. Luukkonen, T. *et al.* Influence of sodium silicate powder silica modulus for mechanical and chemical properties of dry-mix alkali-activated slag mortar. *Constr. Build. Mater.* **233**, 117354. https://doi.org/10.1016/j.conbuildmat.2019.117354 (2020).
66. Zhang, W. *SPSS Statistical Analysis Advanced Tutoria*. 95–106 (2018).
67. Wang, P. *et al.* Prediction of complex strain fields in concrete using a deep learning approach. *Constr. Build. Mater.* **404**, 133257. https://doi.org/10.1016/j.conbuildmat.2023.133257 (2023).
68. Kuang, L., Li, G., Xiang, J., Ma, W. & Cui, X. Effect of seawater on the properties and microstructure of metakaolin/slag-based geopolymers. *Constr. Build. Mater.* **397**, 132418. https://doi.org/10.1016/j.conbuildmat.2023.132418 (2023).
69. Ziada, M., Tanyildizi, H. & Uysal, M. The influence of carbon nanotube on underwater geopolymer paste based on metakaolin and slag. *Constr. Build. Mater.* **414**, 135047. https://doi.org/10.1016/j.conbuildmat.2024.135047 (2024).
70. Trincal, V. *et al.* Effect of drying temperature on the properties of alkali-activated binders - Recommendations for sample precon-ditioning. *Cem. Concr. Res.* **151**, 106617. https://doi.org/10.1016/j.cemconres.2021.106617 (2022).
71. Puertas, F. et al. C-A-S-H gels formed in alkali-activated slag cement pastes. Structure and effect on cement properties and durabil-ity. MATEC Web Conf. 11, 01002 (2014). https://doi.org/10.1051/matecconf/20141101002
72. Liao, Y. *et al.* Hydration behavior and strength development of supersulfated cement prepared by calcined phosphogypsum and slaked lime. *J. Build. Eng.* **80**, 108075. https://doi.org/10.1016/j.jobe.2023.108075 (2023).

## Author contributions
Conceptualization, Z.Y. and C.Q.; methodology, C.Q.; software, Z.Y.; validation, Z.Y., C.Q. and L.L.; formal analysis, C.Q. and L.L.; investigation, C.Q.; resources, Y.Q.; data curation, Z.Y. and C.Q.; writing—original draft preparation, Z.Y.; writing—review and editing, L.L. and Y.Q.; visualization, Z.Y. and J.C.; supervision, L.L.; project administration, L.L. and Y.Q.; funding acquisition, L.L. and Y.Q. All authors have read and agreed to the published version of the manuscript.

## Funding

## Competing interests
The authors declare no competing interests.

## Additional information
**Correspondence** and requests for materials should be addressed to L.L.

**Reprints and permissions information** is available at www.nature.com/reprints.

**Publisher's note** Springer Nature remains neutral with regard to jurisdictional claims in published maps and institutional affiliations.